nature
biotechnology

Functional photoacoustic microscopy for high-resolution and noninvasive *in vivo* imaging

Hao F Zhang[1,3], Konstantin Maslov[1,3], George Stoica[2] & Lihong V Wang[1]

Although optical absorption is strongly associated with the physiological status of biological tissue, existing high-resolution optical imaging modalities, including confocal microscopy[1,2], two-photon microscopy[3,4] and optical coherence tomography[5], do not sense optical absorption directly. Furthermore, optical scattering prevents these methods from imaging deeper than ~1 mm below the tissue surface. Here we report functional photoacoustic microscopy (fPAM), which provides multiwavelength imaging of optical absorption and permits high spatial resolution beyond this depth limit with a ratio of maximum imaging depth to depth resolution greater than 100. Reflection mode, rather than orthogonal or transmission mode, is adopted because it is applicable to more anatomical sites than the others. fPAM is demonstrated with *in vivo* imaging of angiogenesis, melanoma, hemoglobin oxygen saturation (sO$_2$) of single vessels in animals and total hemoglobin concentration in humans.

fPAM (**Fig. 1**) is a hybrid technique that detects absorbed photons ultrasonically through the photoacoustic effect[6]. When a short-pulsed laser irradiates biological tissues, wideband ultrasonic waves (referred to as photoacoustic waves) are induced as a result of transient thermoelastic expansion. The magnitude of the photoacoustic waves is proportional to the local optical energy deposition and, hence, the waves divulge physiologically specific optical absorption contrasts. As optical energy deposition is related to the optical absorption coefficients of pigments, concentrations of multiple pigments can be quantified for functional imaging by varying the laser wavelength.

Because ultrasonic scattering is two to three orders of magnitude weaker than optical scattering in biological tissues[7], ultrasonic imaging can provide better spatial resolution than pure optical imaging when the imaging depth is beyond one optical transport mean-free-path (~1 mm). For the same reason, photoacoustic sources can be localized with high spatial resolution beyond even ~1 mm by the use of a high-frequency focused ultrasonic transducer.

In our fPAM system, 6-ns laser pulses from a tunable dye laser pumped by a Nd:YAG laser are used to generate photoacoustic waves. Laser light at a designated wavelength is delivered through an optical fiber to the fPAM scanner (**Fig. 1**). The energy of each laser pulse is detected by a photodiode for calibration. The laser beam from the fiber passes through a conical lens to provide a ring-shaped area of illumination. It is then weakly focused into the tissue with the focal region coaxially overlapping the ultrasonic focus inside the tissue. In an optically clear medium, the optical focus is 2 mm in diameter, which is much wider than the ultrasonic focus. The optical illumination on the tissue surface is donut shaped with a dark center so that no strong photoacoustic signals are produced there within the ultrasonic field of view. The photoacoustic wave is recorded at each location of the ultrasonic transducer for 2 μs and subsequently converted into a one-dimensional (1D) depth-resolved image (A-scan) based on the sound velocity in soft tissue (1.54 mm/μs). Then, raster scanning of the dual optical-ultrasonic foci in a horizontal (x-y) plane with a step size of 50 μm produces a three-dimensional (3D) image. No signal averaging is performed. In contrast with other forms of photoacoustic tomography[8,9], fPAM works in reflection (backward) mode rather than orthogonal or transmission mode, provides real-time A-scans and requires no inverse algorithm for image reconstruction. Compared with previous confocal photoacoustic imaging[10], fPAM provides much better image quality at greater depth owing to the use of dark-field illumination.

The lateral resolution of fPAM is determined by the focal diameter of the ultrasonic transducer[11], and the axial resolution is inversely related to the bandwidth of the ultrasonic transducer. Therefore, achieving high spatial resolution requires the use of an ultrasonic transducer with a large numerical aperture (NA), a high central frequency and a wide bandwidth. At central frequencies higher than 10 MHz, it is the penetration depth of ultrasound, rather than the penetration depth of light, that limits the maximum imaging depth owing to strong frequency-dependent acoustic attenuation. As a result, both the spatial resolution and the maximum imaging depth of fPAM are scaleable with ultrasonic parameters within the reach of the excitation photons. In the fPAM reported here, the ultrasonic detector (V214-BB-RM, Panametrics; element diameter: 6 mm) has a 50-MHz central frequency and a 70% nominal bandwidth. A home-made spherically focusing lens provides an NA of 0.44, a focal length of 6.7 mm, and a focal zone of 0.3 mm. This fPAM can image objects of 6 μm in diameter with an axial resolution of 15 μm and a lateral resolution of 45 μm in its focal zone[12]. Moreover, an imaging depth of more than 3 mm in live animals has been accomplished (see **Supplementary Fig. 1** online). Deoxyhemoglobin (HbR),
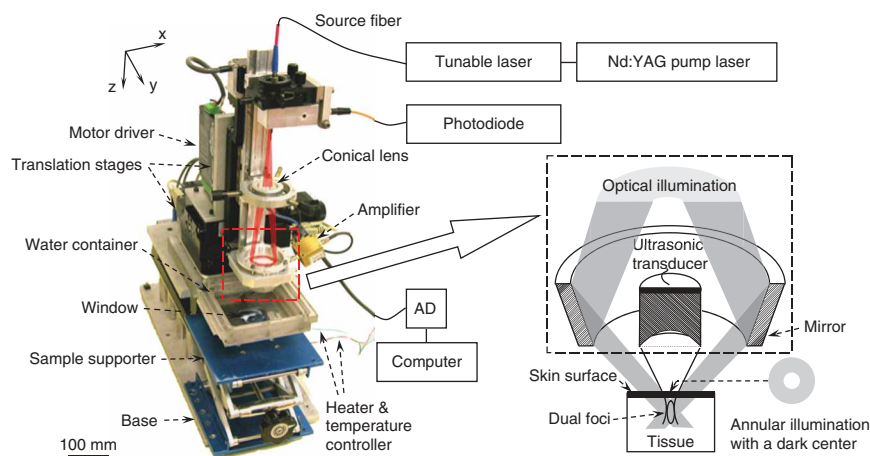
Figure 1 Experimental fPAM system. The components within the dashed box in the photograph are mechanically translated along an x-y plane with the bottom of the mirror and the ultrasonic transducer immersed in water. A window at the bottom of the water container is sealed with an optically and ultrasonically transparent disposable polyethylene membrane (thickness, 0.044 mm). After commercially available ultrasound gel is applied to the region of interest on the sample for acoustic coupling, the sample is placed between the water container and the sample supporter for imaging.

oxyhemoglobin (HbO$_2$) and melanin account for most of the optical absorption in mammalian tissue in the visible spectrum. Consequently, fPAM, which functions as a sensitive blood detector with high contrast and specificity, is suitable for imaging the volumetric morphology of the subcutaneous microvasculature. At the 584-nm isosbestic optical wavelength, where the two forms of hemoglobin have an identical molar extinction coefficient, the contrast of fPAM is sensitive to the total hemoglobin concentration but insensitive to the level of hemoglobin oxygenation. Longitudinal imaging of tumor angiogenesis by fPAM in rats *in vivo* indicates that the tumor exhibits greater vessel complexity and higher microvascular density than the surrounding healthy tissue (see **Supplementary Fig. 2** online). Imaging of angiogenesis by fPAM is potentially useful for understanding tumor growth and metastasis[13], diagnosing cancers and evaluating the efficacy of therapies.

By extending single-wavelength imaging to dual-wavelength imaging, fPAM can separate the contributions from two pigments based on their different absorption spectra. A good example is imaging of melanomas. At 584 nm, fPAM can image the morphological

relationship between a melanoma and the surrounding blood vessels in the x-y view because both melanin and hemoglobin have comparably strong absorptions at this wavelength. However, visible light at this wavelength is not suitable for measuring tumor thickness because it cannot easily penetrate the melanin-rich tumor. Generating another image using 764-nm near-infrared light, which can infiltrate the tumor because of both the decreased optical absorption of melanin and the nearly minimal optical absorption of blood, overcomes this limitation. Combining the two images from these two spectral regions reveals the 3D morphology of both the melanoma and the surrounding vasculature (**Fig. 2**). In the **Supplementary Video 1** online, parallel arterioles and venules are evident. Microvessels with diameters of less than a single pixel (50 μm), presumably resulting from angiogenesis, are seen to surround the melanoma (**Fig. 2b**). At 584 nm, the average ratio of the vessel to the background in photoacoustic signal amplitude is 13 ± 0.89, and the average ratio of this melanoma to the surrounding blood vessels is 0.92 ± 0.02. However, at 764 nm, the average ratio of the melanoma to the blood vessels is 29 ± 3, and the average ratio of the melanoma to the background is 68 ± 5. Such high optical contrast and specificity result from the minimal background absorption and the strong absorption of both hemoglobin and melanin. The average contrast-to-noise ratios for melanoma are 67 dB and 64 dB at 584 nm and 764 nm, respectively. This demonstrates that fPAM can potentially detect and evaluate melanoma.

In addition to the functional imaging of total hemoglobin concentration, fPAM is capable of providing functional imaging of sO$_2$ using multiwavelength measurements[14]. Although the optical measurement of sO$_2$ has been investigated for decades, noninvasive *in vivo* sO$_2$ imaging of single blood vessels has failed owing to either inadequate spatial resolution or low sensitivity. fPAM quantifies sO$_2$ similarly to traditional optical techniques. HbR and HbO$_2$ are treated as the dominant absorbing compounds, and their relative concentrations are calculated on the basis of their molar extinction spectra from spectral measurements of the total absorption coefficient[15]. However,
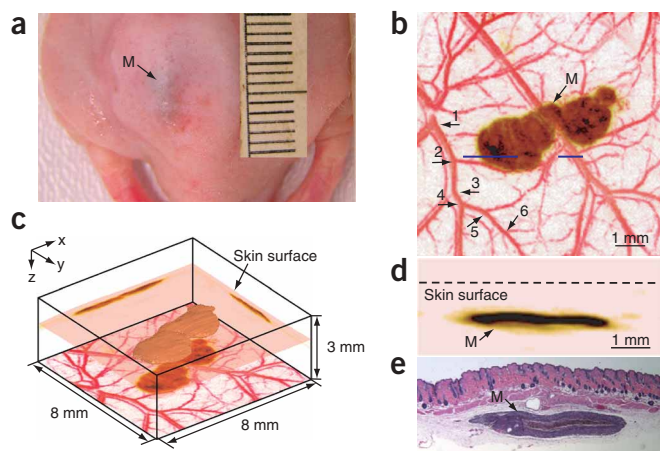
Figure 2 *In vivo* imaging of a subcutaneously inoculated B16-melanoma in an immunocompromised nude mouse using fPAM at 584 nm and 764 nm. (**a**) Photograph of the melanoma. (**b**) A composite of the two maximum-amplitude projection (MAP) images projected along the z axis, where an MAP image is formed by projecting the maximum photoacoustic amplitudes along a direction to its orthogonal plane. Here, blood vessels are pseudo-colored red in the 584-nm image and the melanoma is pseudo-colored brown in the 764-nm image. As many as six orders of vessel branching can be observed in the image as indicated by numbers 1–6. (**c**) Three-dimensional rendering of the melanoma from the data acquired at 764 nm. Two MAP images at this wavelength projected along the x and y axes are shown on the two side walls, respectively. The composite image shown in **a** is redrawn at the bottom. The top surface of the tumor is 0.32 mm below the skin surface, and the thickness of the melanoma is 0.3 mm. (**d**) An enlarged cross-sectional (B-scan) image of the melanoma parallel with the z-x plane at the location marked with a dashed line in **a**. (**e**) Hematoxylin-and-eosin (HE) stained section at the same marked location. M, melanoma.
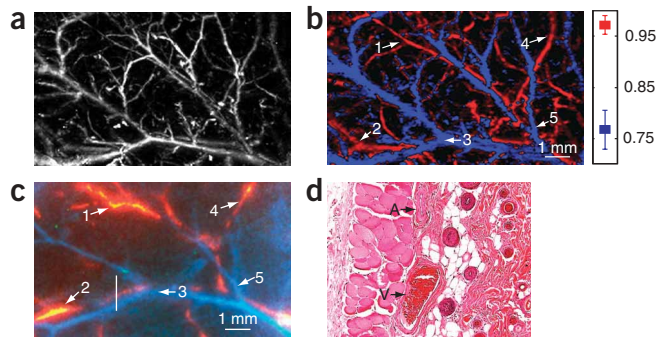
Figure 3 Functional imaging of sO_2 by fPAM *in vivo* in a 150-g Sprague-Dawley rat. Four wavelengths (578 nm, 584 nm, 590 nm and 596 nm) were employed to acquire four different images. (**a**) Structural image acquired at 584 nm. (**b**) Vessel-by-vessel sO_2 mapping based on a least-squares fitting of the four images. The calculated sO_2 values are shown in the color bar. (**c**) Microsphere-perfusion image showing arterioles (red) and venules (blue). The perfusion study was modified from the traditional ink-and-gelatin procedure[20] by replacing the stained gelatin solution with a 1-ml suspension of 20-mg red-fluorescent microspheres. Some vessel features, numbered 1–5, match correctly with those in **b**. This confirms that the vessels with high and low sO_2 measurements are arterioles and venules, respectively. (**d**) HE-stained section showing the vessel structure at the location marked with a dashed line in **c**. The arteriole and venule can be distinguished by their wall thicknesses. A, arteriole; V, venule.

fPAM can pinpoint individual blood vessels with high resolution and evaluate their individual sO_2 levels.

fPAM was first validated by measuring the sO_2 of bovine blood *ex vivo*. The results were consistent with those obtained using a standard optical method[16], with a relative systematic difference between both methods of less than 4% and a minimal detectable variation in sO_2 of 1%. fPAM was then used to image the static sO_2 of subcutaneous vessels in normoxia, where the measured photoacoustic amplitudes from blood vessels were compensated for by the average wavelength-dependent optical attenuation in the dermis. The imaged dimensionless sO_2 measured 0.97 ± 0.02 in arterial blood and 0.77 ± 0.04 in venous blood (**Fig. 3**). Whereas all other techniques measure volume-averaged sO_2, fPAM provides vessel-by-vessel mapping of sO_2 (**Fig. 3b**). This unique feature of fPAM creates an opportunity for the further investigation of, for example, oxygen consumption by tumors.

fPAM was also used to monitor variations in sO_2. From normoxia to hypoxia, the imaged sO_2 levels in venous and arterial blood decrease by 0.096 ± 0.025 and 0.14 ± 0.03, respectively. From normoxia to hyperoxia, the imaged sO_2 levels in venous and arterial blood increase by 0.036 ± 0.031 and 0.012 ± 0.016, respectively. These results indicate that fPAM can potentially image brain functions based on local deoxygenation following intensive neuron firing[17].

fPAM is safe for human subjects as it delivers a fluence of only ~ 6 mJ/cm^2 at the optical focus even for transparent samples. This fluence is well within the ANSI safety standard (20 mJ/cm^2) in the spectral regions used here. An *in vivo* volumetric image of the subcutaneous microvasculature of the palm of a human hand was acquired using fPAM at 584 nm (**Fig. 4**). Total hemoglobin concentration in the palm was imaged with a quality comparable to that in the aforementioned animal studies. The largest vessel in the image is ~ 350 μm in diameter, whereas the smallest is within one pixel (50 μm). The average ratio of the vessel to the background in photoacoustic signal amplitude is 35 ± 2, and the average contrast-to-noise ratio is 51 dB.

Although a 1D scan for a single B-scan image takes only 10 s, a 2D scan over an 8-mm-by-8-mm area takes more than 18 min for single-

wavelength imaging and 160 min for multiwavelength sO_2 imaging. However, because each A-scan is acquired within only 2 μs, fPAM is fundamentally a high-speed technology. The acquisition time of fPAM is currently limited only by the 10-Hz laser pulse repetition frequency and can be potentially increased substantially by using a laser of a higher repetition frequency. Use of an ultrasonic transducer array can further increase the acquisition speed and potentially enable real-time fPAM.

In summary, fPAM has several attractive capabilities. First, it transcends the current depth limit of high-resolution optical imaging modalities while maintaining the depth-to-resolution ratio > 100 (see **Supplementary Table 1** online). Second, the imaging depth and spatial resolution are scaleable without substantially changing the depth-to-resolution ratio. Third, fPAM enables functional imaging based on physiologically specific endogenous optical absorption contrasts. Fourth, fPAM can potentially provide molecular or genetic imaging based on exogenous contrast mechanisms. Fifth, fPAM holds promise for real-time imaging. Finally, fPAM is safe for human subjects, and is likely to be suitable for both clinical application and basic research. Prospective applications for fPAM are in cancer
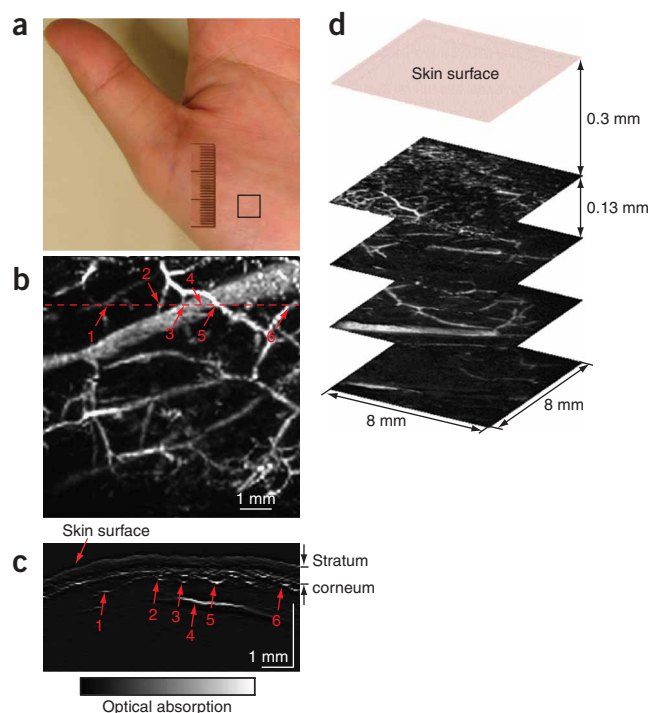
Figure 4 *In vivo* imaging of the total hemoglobin concentration in subcutaneous vasculature of the palm of a human hand by fPAM at 584 nm. (**a**) Photograph of the imaged area. (**b**) MAP image of the photoacoustic signals below the stratum-corneum layer projected along the *z* axis. (**c**) B-scan image in the *z-x* plane at the location indicated by the dashed line in **b**. The skin surface and the stratum corneum as well as blood vessels are visualized. Numbers 1–6 indicate the corresponding vessels in the MAP and B-scan images. (**d**) Series of MAP images from different layers parallel to the skin surface. The first layer starts from 0.17 mm beneath the skin surface, and the layer spacing is 0.13 mm.

research, where angiogenesis is highly correlated with the severity of tumors; in neuroscience, perhaps with the help of cranial windows[18], where sO_2 is related to neural activities; in cancer radiotherapy and chemotherapy, where hypoxia is often responsible for resistance to therapy; in trauma evaluation, where optical absorption is associated with both hemorrhage and edema; and in endoscopic imaging, when miniaturized optical and ultrasonic components are integrated into a single probe.

METHODS

Ethical review of procedures. All experimental animal and human procedures were carried out in conformity with the guidelines of the US National Institutes of Health. The laboratory animal and human protocols for this work were approved by the University Laboratory Animal Care Committee of Texas A&M University.

Experimental animals. Adult Sprague-Dawley rats (Charles River Breeding Laboratories, 150–200 g) and immunocompromised nude mice (Harlan Co., 20 g) were used. Before imaging, the hair on the dorsal sides close to the rear legs was removed with human hair-removing lotion (Surgi Cream, Ardell Int'l). A dose of 87 mg/kg Ketamine and 13 mg/kg Xylasine was administered intramuscularly to anesthetize the rats, and supplemental injections (~50 mg/kg/h) kept the rats motionless throughout the experiments. During the experiments, the arterial blood oxygenation and the heart rates of the animals were monitored by a pulse Oximeter (8600 V, Nonin Medical). After the data acquisition for fPAM, the animals were killed by an intraperitoneal administration of pentobarbital at a dosage of 100 mg/kg.

Inoculation of tumors. In tumor angiogenesis imaging, 0.15 ml of suspension containing 5 million BR_7C_5 tumor cells was subcutaneously inoculated into the Sprague-Dawley rats on the dorsal sides. The BR_7C_5 is a highly metastatic mammary adenocarcinoma cell clone derived from an *N*-ethyl-*N*-nitrosourea-induced mammary tumor in Berlin-Druckrey IV rats[19]. In skin melanoma imaging, 0.05 ml of suspension containing 0.5 million B16 melanoma cells (American Type Culture Collection) was subcutaneously inoculated into the nude mice on the dorsal sides. The cells were cultured in DMEM supplemented with 5% FBS, 2 mM L-glutamine, 100 units/ml penicillin and 100 mg/ml streptomycin (Gibco BRL, Life Technologies) at 37 °C in a humidified atmosphere of 95% air and 5% CO_2.

Intravascular microsphere perfusion. After data acquisition by fPAM in static sO_2 imaging, the rats were kept deeply anesthetized. Then the heart was exposed and an incision was made at the right atrium. A volume of 1 ml fluorescent-microsphere suspension mixed with anticoagulant (citrate dextrose solution) was injected from the left ventricle. The average diameter of the microspheres was 16 μm. After injection into the systemic circulation, the microspheres were clogged in the capillary bed because the diameter of the capillary is <10 μm; thus, they were absent in the venous blood. As a result, good contrast between the arterial blood and venous blood was created for postmortem fluorescence imaging. After the heart had fully stopped beating, skin regions imaged by fPAM were harvested for fluorescence imaging and histology.

Histology. Histological sections stained with hematoxylin-and-eosin were prepared by routine procedures from tissues fixed by immersion in 10% neutral phosphate-buffered formalin.

Note: Supplementary information is available on the Nature Biotechnology website.

COMPETING INTERESTS STATEMENT
The authors declare that they have no competing financial interests.

Published online at http://www.nature.com/naturebiotechnology/
Reprints and permissions information is available online at http://npg.nature.com/reprintsandpermissions/

1. Wilson, T. & Sheppard, C. *Theory and Practice of Scanning Optical Microscopy* (Academic Press, London, 1984).
2. Sipkins, D.A. *et al. In vivo* imaging of specialized bone marrow endothelial microdomains for tumour engraftment. *Nature* **435**, 969–973 (2005).
3. Denk, W., Strickler, J.H. & Webb, W.W. Two-photon laser scanning fluorescence microscopy. *Science* **248**, 73–76 (1990).
4. So, P.T.C., Dong, C.Y., Masters, B.R. & Berland, K.M. Two-photon excitation fluorescence microcopy. *Annu. Rev. Biomed. Eng.* **2**, 399–429 (2000).
5. Huang, D. *et al.* Optical coherence tomography. *Science* **254**, 1178–1181 (1991).
6. Sun, T. & Diebold, G.J. Generation of ultrasonic waves from a layered photoacoustic source. *Nature* **355**, 806–808 (1992).
7. Duck, F.A.. *Physical Properties of Tissue* (Academic Press London, 1990).
8. Wang, X. *et al.* Noninvasive laser-induced photoacoustic tomography for structural and functional *in vivo* imaging of the brain. *Nat. Biotechnol.* **21**, 803–806 (2003).
9. Hoelen, C.G.A., de Mul, F.F.M., Pongers, R. & Dekker, A. Three-dimensional photoacoustic imaging of blood vessels in tissue. *Opt. Lett.* **23**, 648–650 (1998).
10. Oraevsky, A.A. & Karabutov, A.A. Optoacoustic tomography. in *Biomedical Photonics Handbook,* vol. PM125 (ed. Vo-Dinh, T.) (CRC Press, Boca Raton, Florida, 2003).
11. Briggs, G.A.D. *Acoustic Microscopy,* p. 27 (Clarendon, Oxford, 1992).
12. Maslov, K., Stoica, G. & Wang, L.V. In vivo dark-field reflection-mode photoacoustic microscopy. *Opt. Lett.* **30**, 625–627 (2005).
13. Carmeliet, P. & Jain, R.K. Angiogenesis in cancer and other diseases. *Nature* **407**, 249–257 (2000).
14. Jobsis, F.F. Noninvasive, infrared monitoring of cerebral and myocardial oxygen sufficiency and circulatory parameters. *Science* **198**, 1264–1267 (1977).
15. Chance, B. *et al.* Comparison of time-resolved and -unresolved measurements of deoxyhemoglobin in brain. *Proc. Natl. Acad. Sci. USA* **85**, 4971–4975 (1988).
16. Tsao, M.U., Sethna, S.S., Sloan, C.H. & Wyngarden, L.J. Spectrophotometric determination of the oxygen saturation of whole blood. *J. Biol. Chem.* **217**, 479–488 (1955).
17. Vanzetta, I. & Grinvald, A. Increased cortical oxidative metabolism due to sensory stimulation: implications for functional brain imaging. *Science* **286**, 1555–1558 (1999).
18. Levasseur, J., Wei, E., Raper, A., Kontos, H. & Patterson, J. Detailed description of a cranial window technique for acute and chronic experiments. *Stroke* **6**, 308–317 (1975).
19. Hall, D.G. & Stoica, G. Characterization of brain and bone-metastasizing clones selected from an ethylnitrosourea-induced rat mammary carcinoma. *Clin. Exp. Metastasis* **12**, 283–295 (1994).
20. Ambach, G. & Palkovits, M. Blood supply of the rat hypothalamus I. nucleus supraopticus. *Acta Morphol. Acad. Sci. Hung.* **22**, 291–310 (1974).